Low-lying quadrupole and octupole collective excitations in the ^{112,116,118,120,122,124}Sn isotopes

A. Kundu,[1,2,*] S. Santra,[1,2] A. Pal,[1,2] D. Chattopadhyay,[1,2] R. Tripathi,[2,3] B. J. Roy,[1,2] T. N. Nag,[3] B. K. Nayak,[1,2] A. Saxena,[1,2] and S. Kailas[1,2]

[1]*Nuclear Physics Division, Bhabha Atomic Research Centre, Mumbai 400085, India*
[2]*Homi Bhabha National Institute, Anushakti Nagar, Mumbai 400094, India*
[3]*Radiochemistry Division, Bhabha Atomic Research Centre, Mumbai 400085, India*

Background: In recent years, considerable interest has been focused on the study of the effect of neutron skin on the collective properties of vibrational nuclei. This can be best evidenced by exclusively determining neutron and proton transition matrix elements involved in a particular excitation by investigating the Coulomb-nuclear interference feature of inelastic scattering.

Purpose: Measurement of angular distributions of the inelastic scattering cross sections for excitations to low-lying 2_1^+ and 3_1^- states in ^{112,116,118,120,122,124}Sn using ^{7}Li beam as probe at $E_{lab} = 28$ MeV and determination of neutron and proton transition matrix elements involved in each excitation.

Methods: Projectilelike fragments were detected using six sets of Si-surface barrier detector telescopes to measure the cross sections for elastic and inelastic scattering channels. Optical model analysis of elastic scattering data, coupled reaction channels, and continuum discretized coupled channels calculations were performed to understand the measured differential cross sections. An attempt has been made to extract the microscopic mass and charge deformation lengths.

Results: For the 2_1^+ state, experimental $B(E2)$ values are in good agreement with existing results obtained by electromagnetic methods. Charge and mass quadrupole vibrations are homogeneous. Significant differences are observed for excitation to the 3_1^- state across the Sn isotopic chain. Available structural information for collective octupole vibrations could not reproduce the present data for this excitation. Results show much lower values of octupole mass deformation parameters.

Conclusions: Isoscalar nature of surface vibrations for the 2_1^+ state in Sn isotopes is verified, with $M_n/M_p \sim N/Z$. For the 3_1^- state, damped mass vibration is the primary observation. On comparison with existing estimates, a significant deviation from isoscalar nature is conjectured for this excitation, when probed with ^{7}Li.

I. INTRODUCTION

Inelastic transitions in a nucleus are caused by electromagnetic and/or nuclear interactions with a second nucleus. The corresponding transition amplitudes reveal dynamic deformations in the density distribution of the participating nuclei. The formalism of inelastic scattering is primarily decided by the number of units of angular momentum transferred in the process. This determines the multipolarity, λ, of the reaction and demarcates three separate regions where (i) the Coulomb field (long range) dominates, (ii) the Coulomb and nuclear fields interfere, and (iii) the nuclear field (short range) dominates. In the collective model of multipole nuclear vibrations, one thinks of a homogeneous isoscalar neutron-proton fluid undergoing shape oscillations about the equilibrium, with their respective transition densities in the ratio of N/Z. Neutron-excess nuclei with high N/Z ratios may exhibit the unusual feature of decoupled neutron and proton transition densities

due to the presence of neutron skin. In such scenarios, the question of the relative participation of neutron and proton distributions in low-lying collective surface vibrations is of considerable interest. The nature of the different excited states are then best evidenced by looking at the transition parameters. However, these structural parameters of a nucleus are often found to be probe dependent [1]. The ratio of the neutron and proton transition matrix elements, M_n/M_p, has often been used to identify any inhomogeneity between their respective transition strengths, in comparison with the isoscalar value of $M_n/M_p \sim N/Z$ [2]. While proton (or charge) transition matrix element, M_p, can be obtained from electron scattering or Coulomb excitation measurements, the determination of neutron transition matrix element, M_n, requires scattering of light-/heavy-ion probes, whose reaction mechanisms are complex. Excitation in heavy-ion collisions is often induced by energetic ions not too far above the barrier; contributions from Coulomb and nuclear processes thus become comparable as impact parameter varies. At large distances between incoming projectile and target nucleus, Coulomb scattering to forward angles gives reliable structural information that connects theory and experiment. As smaller distances are

———
*ananyak.delhi@gmail.com

approached, the nuclear amplitude changes rapidly causing scattering to backward angles, making it possible to determine Coulomb and nuclear deformations separately by measuring the distribution of scattered particles over a large angular range. The shape of the differential cross section is characterized by a Coulomb-nuclear interference (CNI) pattern, which allows simultaneous determination of electromagnetic (charge or Coulomb) and isoscalar (mass or nuclear) transition parameters, namely deformation lengths, δ_λ^{ch} and δ_λ^m. These are sensitive to deviations in charge (proton) and mass (neutron + proton) distributions from mean spherical shape, respectively, when transitions of multipolarity λ take place. Bernstein *et al.* [1–4] have reviewed various methods to determine M_n/M_p ratios. Comparing pure Coulomb scattering with heavy-ion scattering data is considered as one of the most transparent approaches. However, to avoid large experimental uncertainties of M_n/M_p due to normalization error of heavy-ion cross sections, a simultaneous determination of electromagnetic and isoscalar transition probabilities, for which M_n/M_p is not affected by normalization uncertainties, may be achieved by heavy-ion scattering across the CNI region.

The main objective of this study is to utilize such CNI effects for quantitative assessments of δ_λ^{ch} and δ_λ^m, and deduce the M_n/M_p ratios for the $(0_{g.s.}^+ \rightarrow 2_1^+; \lambda = 2)$ and $(0_{g.s.}^+ \rightarrow 3_1^-; \lambda = 3)$ transitions in ^{112,116,118,120,122,124}Sn using ^{7}Li beam as probe at $E_{lab} = 28$ MeV ($V_B \approx 20$ MeV; $E_{lab}/V_B \approx 1.4$).

In the present study, differential cross sections for elastic and inelastic scattering have been measured. A simultaneous description of these channels has been attempted by means of explicit coupled reaction channels (CRC) as well as continuum discretized coupled channels (CDCC) calculations with a consistent set of structural and potential parameters. The characteristics of the dominant multipole transitions to the low-lying first excited states in Sn isotopes have been frequently studied with a variety of probes such as Coulomb excitation, electron, proton, and α scattering. The $\lambda = 2$ electromagnetic transition probabilities, $B(E2)$, are found to be fairly consistent with one another [5–10] with smaller uncertainties. However, the $\lambda = 3$ transition probabilities, $B(E3)$, have a wide range with larger uncertainties [11–18]. The scattering cross sections for the ^{7}Li + ^{120}Sn system were also reported earlier in Ref. [19]. Extensive measurements using heavy-ion probes and understanding of the basic collective phenomena in low-lying transitions along an isotopic chain of stable neutron-excess nuclei, with better understood structures, could act as a reference for studies with unstable nuclei possessing larger neutron skins, that are expected to be of similar complexity. A fresh study of Coulomb and nuclear inelastic excitation of such stable neutron-excess nuclei is therefore of great interest.

The paper is organized as follows. The experimental setup and the data analysis procedure used to extract the differential cross sections are described in Sec. II. The model calculations using FRESCO [20] that explain the experimental data are described in Sec. III. The method used to arrive at the neutron and proton transition matrix elements is highlighted in Sec. IV, and finally, the results are discussed and summarized in Sec. V.

II. MEASUREMENT AND DATA ANALYSIS

The angular distributions for elastic and inelastic scattering cross sections were measured at the Pelletron accelerator facility, Mumbai. Self-supporting enriched (>95%) Sn targets were used of thicknesses $\approx$540 μg/cm^2(^{112}Sn), $\approx$1.45 mg/cm^2(^{116}Sn), $\approx$320 μg/cm^2(^{118}Sn), $\approx$280 μg/cm^2 (^{120}Sn), $\approx$85 μg/cm^2(^{122}Sn), and $\approx$290 μg/cm^2(^{124}Sn). Six telescopes (ΔE-E) of Si-surface barrier detectors, placed 10° apart on one arm of a scattering chamber at a distance of $\approx$21 cm each from the target center, were used to detect projectilelike fragments in the angular range of 25°–140°. Two other Si-surface barrier detectors fixed at 20° and 30° with respect to the beam on another arm at a distance of $\approx$39 cm from the center, were used for flux normalization. The detector thicknesses were 25–50 μm for ΔE and $\approx$1000 μm for the E detectors. The schematic experimental arrangement is same as that shown in Fig. of Ref. [19]. From a typical gain-matched spectrum of ΔE versus $E_{total}(=E + \Delta E)$ shown for the ^{7}Li + ^{122}Sn system in Fig. 1, fragments with different $Z(=1$–$3)$ and $A(=1$–$7)$ are clearly identified. Typical energy resolution of a telescope was $\approx$60 keV. Along with the elastic scattering peak, the yields of projectile and target excited states corresponding to first quadrupolar rotational state of ^{7}Li (0.478 MeV), and the 2_1^+ and 3_1^- vibrational states of ^{112,116,118,120,122,124}Sn were found to be dominant (see inset of Fig. 1). In addition, several states corresponding to one-neutron stripping (^{7}Li, ^{6}Li) as well as one-proton stripping (^{7}Li, ^{6}He), with subsequent excitation of the respective residual nuclei could be identified.

The background-subtracted yields for the elastic scattering and excited (2_1^+ and 3_1^-) states of target were extracted separately for evaluating their differential cross sections, which were translated to the center-of-mass frame. The experimental cross sections for scattering to the 2_1^+ excited state for each Sn isotope are shown as open squares in Figs. 2(a)–2(f),
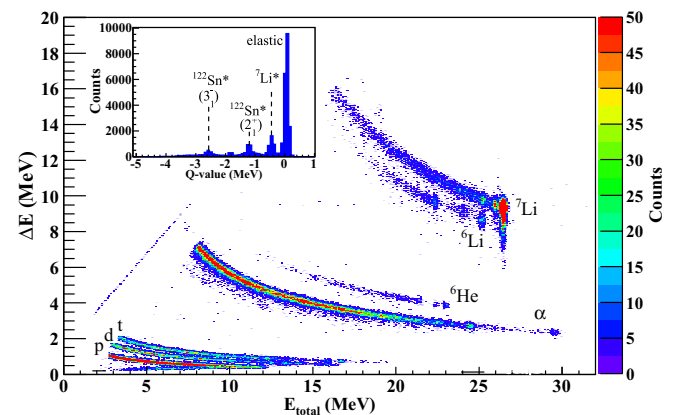

FIG. 1. Typical two-dimensional (ΔE versus E_{total}) gain-matched spectrum showing the outgoing projectilelike fragments at $\theta_{lab} = 60°$ in the ^{7}Li + ^{122}Sn system. Colour gradient scale given on the right side of the plot represents number of correlated events in both ΔE and E detectors. Inset: One-dimensional spectrum showing Q-value distribution of states identified in elastic and inelastic scattering.
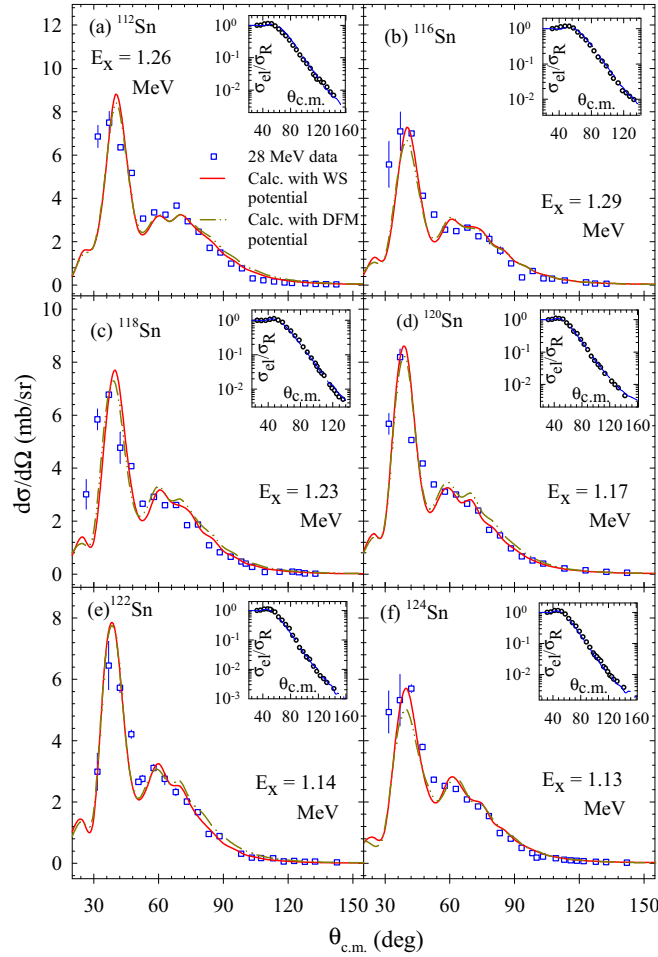
FIG. 2. Experimental cross sections (open squares) and the results of the CRC calculations (solid lines for WS potential, dash-dot-dot lines for DFM potential) for $\lambda = 2$ inelastic scattering processes corresponding to the target excitations in $^7\text{Li} + {}^{112,116,118,120,122,124}\text{Sn}$ systems. Inset: Experimental elastic scattering angular distributions (circles) with calculation using WS potential (dashed lines).
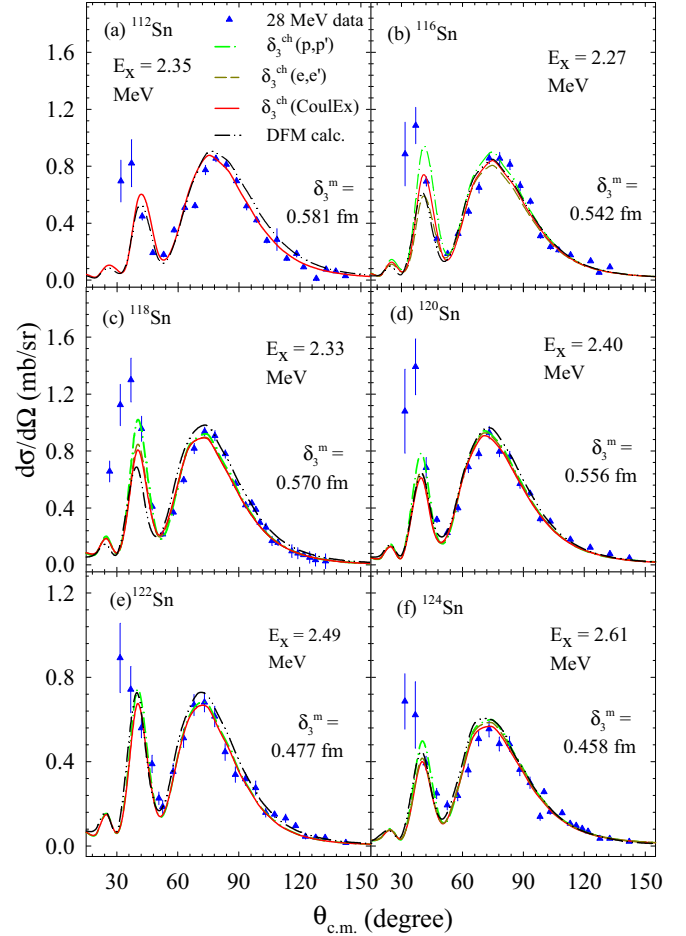
FIG. 3. Experimental cross sections (filled triangles up) and the results of the CRC calculations (lines) for $\lambda = 3$ inelastic scattering processes corresponding to the target excitations in $^7\text{Li} + {}^{112,116,118,120,122,124}\text{Sn}$ systems. Calculations using WS potential with δ_3^{ch} values from existing Coulomb excitation measurement [11] (solid lines), electron scattering [13,14] (dashed lines), and proton scattering [15] (dash-dot lines) are shown. Also shown are calculations using DFM potential with δ_3^{ch} from Coulomb excitation (dash-dot-dot lines).

with the elastic scattering angular distributions in the inset (open circles). The average statistical errors on the elastic scattering cross sections are typically 2–3 % over the entire angular range. The $\lambda = 2$ transition is found to be dominant in the forward region where Coulomb field is expected to have greater influence than nuclear field. Figures 3(a)–3(f) shows the experimental differential cross sections for inelastic excitation to the 3_1^- state (triangles). The lines in all figures represent the results of the CRC calculations described in Sec. III A.

III. THEORETICAL CALCULATIONS

A. CRC calculations

CRC calculations were performed using FRESCO by coupling the major direct reaction channels to the entrance channel. The target excited states were treated as collective vibrational states. The distorted waves were generated from a phenomenological optical potential of Woods-Saxon (WS)

volume type, whose parameters were determined by reproducing the measured elastic scattering data for each system. This may be considered as the local equivalent potential (i.e., bare + polarization potential) that has taken care of the effect of couplings of breakup and other excluded reaction channels on the elastic channel. The total potential is defined as:

$$V_{\text{total}}(r) = V_c(r, r_c) - \frac{V_0}{1 + \exp\left(\frac{r - r_0}{a_0}\right)} - \frac{iW_0}{1 + \exp\left(\frac{r - r_w}{a_w}\right)}.$$

(1)

Here, $V_c(r, r_c)$ is the Coulomb potential due to a uniformly charged sphere of radius $R_c = r_c(A_P^{1/3} + A_T^{1/3})$, with charge radius r_c fixed at 1.20 fm and A_P and A_T are the mass numbers of projectile and target, respectively. The mass radius is calculated as an average of r_0 and r_w. The depth of the real part was adjusted to optimize the simultaneous fit to

elastic and inelastic scattering cross sections in each system. The volume absorptive imaginary part accounted for flux lost into the excluded nonelastic channels, as well as compound reaction in the entrance channel. To arrive at a consistent set of nuclear potential parameters across the Sn isotopic chain, two of the six parameters (r_0 and a_0) were kept fixed and the ranges of the others were restricted.

For constraining the set of potential and target structural parameters, inelastic excitation of ^{7}Li to its only bound quadrupolar rotational state $\frac{1}{2}^-$ at 478 keV was also coupled into the model calculations with $\delta^{ch} = 3.944$ fm (obtained using ground-state spectroscopic quadrupole moment -4.06 e fm^2 and $B(E2;\ 3/2^- \rightarrow 1/2^-) = 8.3$ e^2 fm^4 and $\delta^m = 1.993$ fm, as measured earlier in Ref. [19]. This mass deformation length is consistent with the one obtained from an earlier measurement on ^{7}Li + ^{11}B, ^{13}C systems [21]. However, it may be important to note that in the work of Ref. [21] the relative heights of the maxima observed in the differential cross section could not be reproduced with the parameters $\delta^m = \delta^{ch} = 2.0$ fm. In the present work, the nuclear contribution to the inelastic excitation of this state is found to be smaller compared to the Coulomb contribution, i.e., $\delta^m < \delta^{ch}$. A similar feature of larger Coulomb amplitude is also observed in Ref. [22]. The present set of calculations could also satisfactorily explain the existing data for ^{7}Li* (0.478 MeV) + ^{120}Sn (g.s.) at a higher bombarding energy [23], as shown previously in Ref. [19]. To find the suitability of the values of δ^{ch} and δ^m for the bound excited state of ^{7}Li to be used in CRC and CDCC calculations, different sets of calculations with unequal as well as similar charge and mass deformation lengths are compared with experimental data (symbols) in Fig. 4. The solid line represents the CRC calculation with unequal deformation lengths for mass and charge densities ($\delta^{ch} = 3.94$ fm and $\delta^m = 2.0$ fm), whereas, the dashed line corresponds to the CRC calculations using equal deformation lengths, i.e., $\delta^m = \delta^{ch} = 2.0$ fm. The dashed-dotted line corresponds to the result of CDCC calculations described later in Sec. III B. Since the solid and dashed-dotted lines reasonably reproduce the experimental data, the respective parameters for ^{7}Li excitation have been used for CRC and CDCC calculations.

In addition, some of the dominant states identified experimentally corresponding to one-nucleon transfer processes with residual excitation up to ≈ 2 MeV were included with available spectroscopic factors [24–26]. The exit channel real potential was kept to be same as that of the entrance channel, with a short-range imaginary potential of WS squared form. The coupling scheme for each system is similar to that described in Ref. [19]. The final potential parameters are listed in Table I. Integrating the radial wave functions up to 50 fm in steps of 0.25 fm and summing over 100 partial waves were found to be adequate to attain numerical convergence.

The measured inelastic scattering angular distributions were reproduced by collective model calculations. In most macroscopic models such as FRESCO, the collective modes are considered as vibrations of the nuclear surface and are associated with the deformation of the charge and/or mass density, usually described in terms of the derivative of the
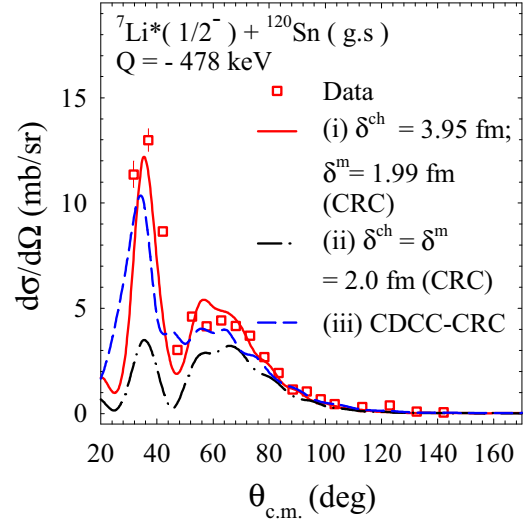

FIG. 4. Experimental cross sections (hollow squares) for inelastic scattering corresponding to bound excited state of ^{7}Li in ^{7}Li + ^{120}Sn system. The lines show CRC calculations for different pairs of δ^{ch} and δ^m values : (i) $\delta^{ch} = 3.944$ fm, $\delta^m = 1.993$ fm (solid), (ii) $\delta^{ch} = \delta^m = 2.0$ fm (dash-dotted), and (iii) CDCC-CRC calculations (dashed) with $B(E2; 3/2^- \rightarrow 1/2^-) = 8.39$ e^2 fm^4 (see text). Calculations for (i) and (iii) are found to suitably agree with the data and these parameters are used for complete theoretical modeling in the CRC and CDCC-CRC frameworks, respectively.

ground-state density of a nucleus. The form factors for inelastic excitations are expressed in terms of the derivative of the phenomenological potential governing elastic scattering of the colliding nuclei, with multiplicative free parameters known as the deformation lengths. The present calculations made use of independent adjustment of charge and mass deformation lengths, δ_λ^{ch} and δ_λ^m (owing to CNI) to reproduce the first and second peak respectively, in Figs. 2(a)–2(f) and Figs. 3(a)–3(f), as well as angular position of the minimum between them. For the $\lambda = 2$ transition in each isotope, δ_2^{ch} is consistent with existing Coulomb excitation measurements of $B(E2)$ [5–10] while δ_2^m differs by only ≈ 2–3 %. The calculations are shown by solid lines in Figs. 2(a)–2(f). For the $\lambda = 3$ transition, however, existing $\delta_3^{ch,m}$ values measured with different probes employing either electromagnetic or nuclear fields [11–13,15–17,27], could not reproduce the data

TABLE I. WS potential parameters for entrance channel used in CRC calculations. Values of r_0 and a_0 have been kept fixed at 1.243 fm and 0.695 fm, respectively.

Target	V_0 (MeV)	W_0 (MeV)	r_w (fm)	a_w (fm)
^{112}Sn	26.05	55.30	1.134	0.620
^{116}Sn	29.25	59.50	1.166	0.575
^{118}Sn	33.66	54.20	1.147	0.605
^{120}Sn	35.06	57.71	1.138	0.678
^{122}Sn	32.05	59.20	1.157	0.571
^{124}Sn	31.45	58.70	1.165	0.605

TABLE II. Experimental deformation lengths for the low lying $\lambda = 2, 3$ excitations in Sn isotopes.

Nucleus	$\lambda = 2$		$\lambda = 3$	
	δ_2^{ch} (fm)[a]	δ_2^m (fm)[a]	δ_3^{ch} (fm)[b]	δ_3^m (fm)[a]
^{112}Sn	0.702(35)	0.698(35)	0.738(103)	0.581(51)
^{116}Sn	0.651(41)	0.656(38)	0.745[c]	0.542(52)
^{118}Sn	0.645(33)	0.651(33)	0.753(108)	0.570(48)
^{120}Sn	0.660(29)	0.642(41)	0.717(129)	0.556(30)
^{122}Sn	0.615(31)	0.611(42)	0.655[c]	0.477(41)
^{124}Sn	0.569(26)	0.563(41)	0.632(087)	0.458(33)

[a]Present measurement.
[b]From Coulomb excitation measurement [11].
[c]Modified.

throughout the angular range. Large inconsistency also exists among measurements with the same probe at different incident energies [13,14,16,17]. The deformation lengths extracted from several existing measurements were found to overestimate the cross section beyond the CNI region. For obtaining the best fit, this was remedied by keeping $\delta_3^{ch} \gg \delta_3^m$ in the present calculations. The results of the calculations reflected a strong correlation between δ_2^m and δ_2^{ch}, whereas δ_3^m was found to be nearly independent of δ_3^{ch}, and determined independently and exclusively from the present data. However, these values are lower than the range of those previously observed over the years. The first maximum of the differential cross section could not be well reproduced, and different sets of calculations are shown in Figs. 3(a)–3(f) keeping δ_3^m fixed and with δ_3^{ch} measured via Coulomb excitation (solid lines) [11], electron scattering (dashed lines) [13,14], and proton scattering (dash-dotted lines) [15], wherever available. The extracted $\delta_\lambda^{ch,m}$ values that provide best reproduction of the present experimental data are presented in Table II. The results reported here involve δ_3^{ch} values deduced from a systematic measurement of Coulomb excitation [11], which is fairly closer to the data compared to other estimates and is extracted purely under the influence of the electric field. Reference [11], however, reports much larger values for ^{116,122}Sn compared to neighboring isotopes. As the calculations were found to be less sensitive to δ_3^{ch}, these values were suitably adjusted for ^{116,122}Sn to obtain a uniform set across the isotopic chain.

1. Sensitivity of optical potential

To test the dependence of the inelastic coupling parameters on the chosen phenomenological potential, the exercise was repeated with different sets of optical potential parameters for each isotope. This was achieved by varying the depth of the real part between 20.0 MeV and 65.0 MeV, imaginary depth between 25.0–60.0 MeV, real radius between 1.20–1.25 fm, imaginary radius between 1.15–1.25 fm, and the diffuseness parameters were varied between 0.60–0.70 fm each. The description of the experimental elastic scattering angular distribution was taken as the reference in each case. The inelastic scattering distribution, however, could be well reproduced with the same set of $\delta_\lambda^{ch,m}$ as indicated in Table II. In particular, the location of the second maximum as well as

the angular position of the first rapid falloff of the differential cross section remain unchanged. The combination of real and imaginary radii required to explain the elastic scattering data always led to similar δ_λ^m irrespective of whether $r_0 < r_w$ or $r_0 > r_w$. In order to compare the calculations using the phenomenological potential with a universal potential, the CRC calculations were repeated with density-dependent double folding model (DFM) nucleus-nucleus potential calculated for systems with at least one spinless nucleus, as a function of center to center separation, r, as

$$V_{DFM}(\mathbf{r}) = \int d\mathbf{r}_1 \int d\mathbf{r}_2 \left[v_{IS}(\mathbf{r} + \mathbf{r}_2 - \mathbf{r}_1) . (\rho_{g.s.}^{1n} + \rho_{g.s.}^{1p}) \right.$$
$$. (\rho_{g.s.}^{2n} + \rho_{g.s.}^{2p}) + v_{IV}(\mathbf{r} + \mathbf{r}_2 - \mathbf{r}_1) . (\rho_{g.s.}^{1n} - \rho_{g.s.}^{1p})$$
$$\left. . (\rho_{g.s.}^{2n} - \rho_{g.s.}^{2p}) \right] \tag{2}$$

Here, v_{IS} and v_{IV} are the radial isoscalar (spin and isospin independent) and isovector (isospin-dependent) parts of the fundamental microscopic nucleon-nucleon interaction parametrized in the M3Y Paris form [28,29], and folded over the particle densities. The shapes of the proton and neutron ground-state densities $\rho_{g.s.}^{(p,n)}$ of the projectile (1) and target (2) were taken to be analogous to their ground-state charge density distributions obtained from existing electron scattering measurements [30], with their r.m.s. radii consistent with the measured neutron skin thickness of the ^{7}Li [31] and Sn nuclei [32,33]. A complex form of the bare DFM potential was used in the full CRC calculations with adjustable normalization factors for the real and imaginary parts, to generate optimum description of elastic scattering (not shown here) and all excited states with the same structural parameters as used earlier. The calculations with DFM have been shown by dash-dot-dot lines for the 2_1^+ state in Figs. 2(a)–2(f) as well as for the 3_1^- state in Figs. 3(a)–3(f). The results are in good agreement with those of the WS potential.

2. Model dependence

To justify the validity of the theoretical calculations in predicting much lower values of δ_3^m compared to various existing estimates, and rule out any model dependence, a reanalysis for few sets of existing data on elastic and $\lambda = 3$ inelastic scattering cross sections for an Sn isotope with different probes, namely p [15], ^{3}He [18], α [17], ^{6}Li [27], was carried out using FRESCO. The potential parameters, number of channels and coupling parameters such as deformation lengths are kept same as in the original measurements. The calculations are done similar to the procedure followed for the present study. The inelastic scattering data (open triangles) and resulting calculations (dashed lines) for the 3_1^- excitation in ^{116}Sn are shown in Figs. 5(a)–5(d) with a good agreement between them. The fit to elastic scattering data has also been reproduced for each system (see insets of Fig. 5). Similar results are observed for existing data on other isotopes of Sn as well. The data is found to be sensitive to δ_3^{ch} mainly in the forward region, though the sensitivity is low. Beyond that, sensitivity depends on δ_3^m, as also observed in the present work. The above exercise rules out any dependence on the
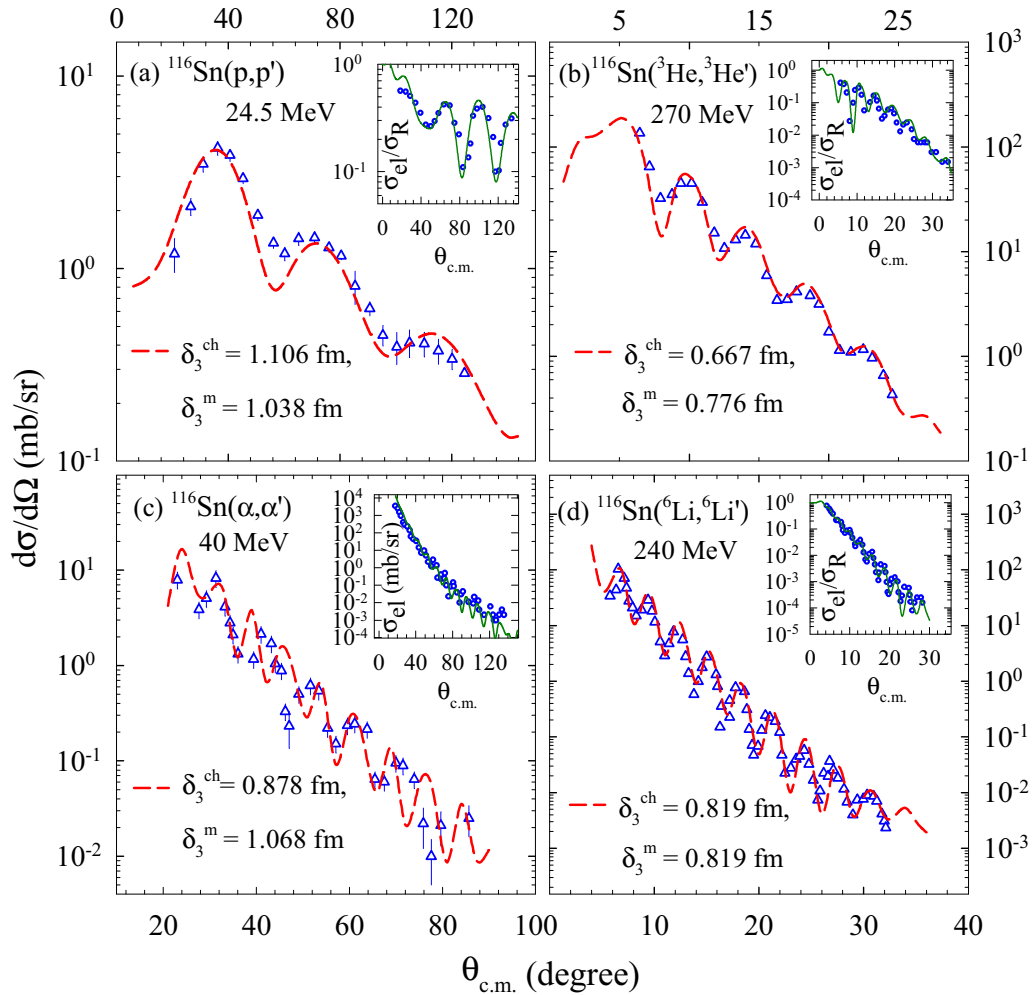
FIG. 5. Experimental cross section (hollow triangles) and calculation (dashed lines) for $\lambda = 3$ inelastic scattering process in (a) p+^{116}Sn [15], (b)^{3}He + ^{116}Sn [18], (c) α + ^{116}Sn [17], and (d)^{6}Li + ^{116}Sn [27] systems. Inset: elastic scattering angular distribution (circles) and respective calculation (solid lines).

coupled channels model employed in the present calculations to predict the values of δ_3^m independently.

B. CDCC-plus-CRC calculations

To further investigate the role of the weakly bound nature of the projectile (if any) in obtaining the low values of δ_3^m in the Sn targets, another set of calculations, the CDCC (continuum discretized coupled channels)-plus-CRC that include a simultaneous analysis of projectile breakup, target collective excitations, and transfer processes, have also been carried out. The coupling of direct and resonant breakup channels of ^{7}Li, which is known to affect the elastic scattering, may in turn affect the target excitation channels that we are interested in. In addition, direct coupling of the projectile breakup channels with the target excitations may also affect the inelastic scattering cross sections. Simultaneous inclusion of both projectile breakup and target inelastic channels has been made by first calculating the cluster-folded (CF) bare potential [34] from the fragment-target interaction potentials. Then, this CF potential has been read in to calculate the

additional potentials contributed by the target deformations corresponding to different excitations.

The projectile excitations corresponding to the bound excited state (0.478 MeV, $1/2^-$), unbound resonant states at 4.63 MeV ($7/2^-$), 6.67 MeV ($5/2^-$), and nonresonant continuum above breakup threshold ($E_{th} = 2.47$ MeV) up to an excitation energy of about 8 MeV of ^{7}Li were included, where it has been assumed to have a cluster structure of $\alpha + t$. The Watanabe-type folding model is assumed for the structure of ^{7}Li as an $\alpha + t$ two-body cluster [35]. This calculates the electromagnetic (charge) as well as nuclear (mass) transition strengths among the excited states of ^{7}Li from the resulting wave functions. The transition potentials are calculated by folding the α and t optical potentials over the ^{7}Li cluster wave functions for the initial and final states, in a similar way to the deformed diagonal potentials as in a conventional collective model calculation. This narrows down to the target structural factors as the only adjustable parameters in the model. The corresponding calculation for excitation to the 0.478 MeV state of ^{7}Li with established $B(E2; 3/2^- \rightarrow 1/2^-) = 8.3$ e^2 fm^4, is shown as dashed lines in Fig. 4.

TABLE III. α-t binding potentials of the form $V = -V_0 e^{-r^2/a_0^2} + V_{so} e^{-r^2/a_{so}^2}$ for the ^{7}Li projectile used in CDCC+CRC calculations.

State(s)	V_0 (MeV)	a_0 (fm)	V_{so} (MeV)	a_{so} (fm)
g.s.+nonresonant	83.780	2.590	2.006	2.590
bound inelastic	83.557	2.570	2.006	2.570
$7/2^-$	83.404	2.520	4.012	2.520
$5/2^-$	78.810	2.520	4.012	2.520

A standard entrance channel projectile-target cluster-folded (CF) interaction was generated, where Sao Paulo potentials [36] were used as the real parts of the fragment-target, $\alpha + $ Sn and $t + $ Sn potentials, evaluated at $E_\alpha = \frac{4}{7}E_{\text{lab}}$ and $E_t = \frac{3}{7}E_{\text{lab}}$. The imaginary potentials were of Woods-Saxon form with short ranged volume and surface terms. The continuum of the α-t cluster of ^{7}Li at excitation $E_x > E_{\text{th}}$ has been discretized with respect to the α-t relative momentum of $\hbar k$ into several momentum bins, in steps of $\Delta k = 0.2$ fm^{-1}, up to $k = 0.8$ fm^{-1} [37]. Each bin beyond E_{th} has been treated as an excited state of the α-t cluster with excitation energy equal to the mean excitation value for that bin. The spin of each excited state has been obtained as the vector sum of the α-t relative angular momentum L and the spin of the triton S. All possible states with $L = 0,1,2,3$ have been included. The binning of the continuum with $L = 3$ has been suitably modified to include the resonances $7/2^-$ and $5/2^-$ with average excitation energies (above E_{th}) of $E_x = 2.16$ and $E_x = 4.21$ MeV, and widths of 0.2 and 3.0 MeV respectively. The α-t binding potentials are of Gaussian form as given in Ref. [38], but suitably adjusted to reproduce the ground-state quadrupole moment and $B(E2; 3/2^-_{\text{g.s.}} \rightarrow 1/2^-_{0.478\,\text{MeV}}))$ for ^{7}Li, as well as generate resonance criteria (phase shift) at correct excitation energies (see Table III). The quadrupole and octupole target excitations were then coupled to the bound and unbound excitations of the projectile by deforming the entrance channel Coulomb and CF interactions with suitable δ_λ^{ch} and δ_λ^m parameters, respectively. Few dominant one-nucleon transfer channels have also been coupled. The strongly coupled elastic, breakup, and inelastic scattering channels were solved exactly and blocked together to be treated as a single unit during iterations. The weaker transfer couplings were treated as successive perturbations iteratively, with exit channel potentials and couplings as mentioned in Sec. III A. The fragment-target São Paulo potentials were normalized suitably to reproduce the elastic scattering angular distribution for each system.

The inelastic scattering data and resulting calculations (solid lines) for the 3^-_1 excitation are shown in Fig. 6 with a good agreement between them in the regions of the valley and the second maximum. The fit to elastic scattering data has also been reproduced for each system (insets of Fig. 6). Interestingly, the data could again be reproduced with the same set of $\delta_3^{ch,m}$ as indicated in Table II which were obtained from CRC analysis described earlier in Sec. III A. In addition, calculations were also performed with lower values of δ_3^{ch} but equal to the respective values of δ_3^m as shown by dashed lines. However, the latter calculations lead to larger disagreement
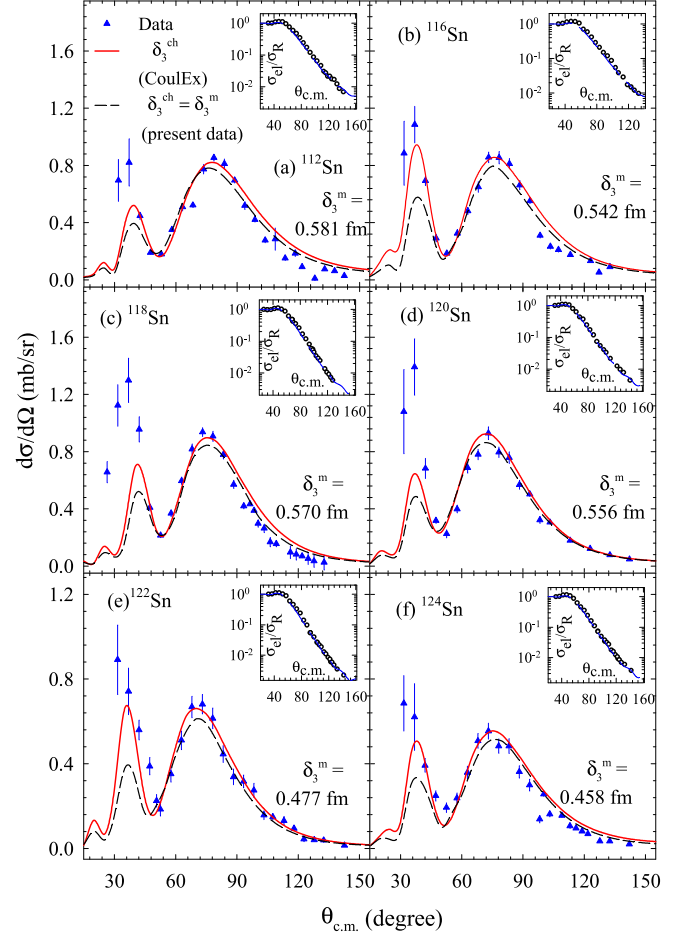

FIG. 6. Experimental cross sections (filled triangles up) and the results of the CDCC-plus-CRC calculations (solid lines) for $\lambda = 3$ inelastic scattering processes corresponding to target excitations in ^{7}Li + ^{112,116,118,120,122,124}Sn systems. Inset: Experimental elastic scattering angular distribution (circles) with calculation under CDCC-CRC formalism (dashed lines). The calculations for inelastic scattering with reduced values of δ_3^{ch} but equal to δ_3^m are also shown (dashed lines).

between experiment and theory in the region of the first maximum. These tests put emphasis on the validity of the realistic coupling parameters and structural information, particularly mass deformation length, extracted using the model calculations for the present systems. The choice of charge deformation length, however, remains ambiguous. Hence, for completeness, the further analysis to probe the interplay between charge and mass vibrations in Sn is carried out using δ_3^{ch} values deduced from existing Coulomb excitation measurement [11].

IV. TRANSITION MATRIX ELEMENTS

From the experimental information of δ_λ^m and δ_λ^{ch}, the exclusive contributions of neutrons and protons can be decoupled in each transition. This is achieved by extracting the corresponding microscopic deformation lengths, $\delta_\lambda^{(n,p)}$, involved in the excitations as described in Refs. [39,40]. A transparent

TABLE IV. Experimental values of microscopic proton and neutron transition parameters obtained from present measurements corresponding to $\lambda = 2$ transition.

Nucleus	N/Z	$\delta_2^{ch} = \delta_2^{p}$ (fm)	δ_2^{n} (fm)	M_n/M_p	$B(E2)$ (e^2b^2)	$B(IS2)$ (e^2b^2)
^{112}Sn	1.24	0.702(35)	0.694(69)	1.25(12)	0.239(9)	0.241(28)
^{116}Sn	1.32	0.651(41)	0.659(70)	1.36(15)	0.207(6)	0.211(18)
^{118}Sn	1.36	0.645(33)	0.655(65)	1.41(09)	0.205(7)	0.214(18)
^{120}Sn	1.40	0.660(29)	0.629(73)	1.38(10)	0.215(9)	0.209(21)
^{122}Sn	1.44	0.615(31)	0.606(73)	1.46(11)	0.191(4)	0.189(15)
^{124}Sn	1.48	0.569(26)	0.558(68)	1.51(08)	0.165(4)	0.166(14)

approach to deduce isospin dependence requires both (p, p') and (n, n') scattering data available at the same energy. But heavy-ion scattering is a reliable substitute. Empirically, it is often assumed [1,2] that $\delta_\lambda^p \sim \delta_\lambda^{ch}$ and $\delta_\lambda^m \sim \frac{Zb_p\delta_\lambda^p + Nb_n\delta_\lambda^n}{Zb_p + Nb_n}$, where $b_{n(p)}$ are microscopic bare interactions of the external field (^{7}Li) with the neutrons (protons) of the Sn isotopes. The ratio b_n/b_p is deduced from the DFM calculations for the isoscalar and isovector parts of the effective nucleus-nucleus potential [18,40], and is ≈ 1 for the present case of heavy-ion systems having a much smaller isospin-dependent interaction compared to the isoscalar part, as expected [28].

The deduced $\delta_\lambda^{(n,p)}$ values are summarized in Tables IV and V. The neutron and proton multipole transition matrix elements are commonly written as

$$M_{(n,p)} = \int_0^\infty r^{\lambda+2} \rho_{tr,\lambda}^{(n,p)} dr \propto (N, Z)\delta_\lambda^{(n,p)} \langle r^{\lambda-1} \rangle_{n,p}, \quad (3)$$

where the corresponding transition densities of a 2^λ-pole excitation are derived using Bohr-Mottelson prescription [41] given by $\rho_{tr,\lambda}^{(n,p)} = -\delta_\lambda^{(n,p)} \frac{d\rho_{g.s.}}{dr}$. The radial momenta $\langle r^{\lambda-1} \rangle_{n,p}$ are taken over the g.s. densities. The ratio of the matrix elements $M_n/M_p = \frac{N\langle r^{\lambda-1}\rangle_n \delta_\lambda^n}{Z\langle r^{\lambda-1}\rangle_p \delta_\lambda^p}$ acts as a realistic tool for identifying the relative participation of neutrons and protons in a collective mass vibration. If the transitions are pure isoscalar with homogeneous mass vibrations, neutron and proton densities are expected to have the same radial shape and one would obtain $\delta_\lambda^n = \delta_\lambda^p$. Any deviation may imply inhomogeneity in a transition. Here, the underlying assumption is that proton and

neutron densities are proportional to each other with Z and N factors.

The results of the present work are summarized in Tables IV and V as well as in Fig. 7. For $\lambda = 2$ transitions, it can be observed from Table IV and Fig. 7(a) that the M_n/M_p ratios (red filled diamonds) agree very well with the homogeneous collective model predictions (N/Z) represented by the dotted line. However, for transition to the 3_1^- states (Table V), with unequal mass and charge deformation lengths (that provide best reproduction of inelastic scattering cross sections), the M_n/M_p ratios are found to be much smaller compared to the collective model predictions (N/Z), as shown as blue filled stars in Fig. 7(b), with no previous measurement. From the present experimental data for inelastic scattering, the values obtained for δ_3^m were unambiguous, whereas, the ones for δ_3^{ch} have large tolerances. Hence, the M_n/M_p ratios become highly sensitive to the choice of δ_3^{ch}. To highlight this, the ratios obtained for $\delta_3^{ch} = \delta_3^m$ are also shown as open circles in Fig. 7(b), which agree with the homogeneous N/Z line, as expected.

The results have been compared with microscopic calculations [dashed and dash-dot-dotted lines in Figs. 7(a) and 7(b)] employing quasiparticle random phase approximation (QRPA) [42] within the quasiparticle-phonon model [43] that accounts for the fact that the proton system in Sn is closed (magic) and the neutron one is not (nonmagic) and collectivity is largely caused by neutrons. The calculations corresponding to both $\lambda = 2$ as well as $\lambda = 3$ transitions lead to the M_n/M_p ratios to be much larger than N/Z. Since the QRPA result is mainly dependent on the neutron density and it does not incorporate the effect of the interplay between electromagnetic

TABLE V. Experimental values of microscopic proton and neutron transition parameters corresponding to $\lambda = 3$ transition obtained from present measurements and Coulomb excitation measurements.

Nucleus	N/Z	$\delta_3^{ch} = \delta_3^{p}$ (fm)[a]	δ_3^{n} (fm)[b]	M_n/M_p[b]	$B(E3)$ (e^2b^3)[a]	$B(IS3)$ (e^2b^3)[b]
^{112}Sn	1.24	0.738(103)	0.453(93)	0.79(13)	0.087(12)	0.058(11)
^{116}Sn	1.32	0.745[c]	0.392(71)	0.73(10)	0.095[c]	0.053(08)
^{118}Sn	1.36	0.753(108)	0.434(95)	0.82(15)	0.097(14)	0.059(10)
^{120}Sn	1.40	0.717(129)	0.439(99)	0.91(15)	0.090(17)	0.057(11)
^{122}Sn	1.44	0.655[c]	0.353(66)	0.82(11)	0.077[c]	0.043(08)
^{124}Sn	1.48	0.632(087)	0.338(65)	0.85(13)	0.073(10)	0.040(07)

[a]From Coulomb excitation measurement.
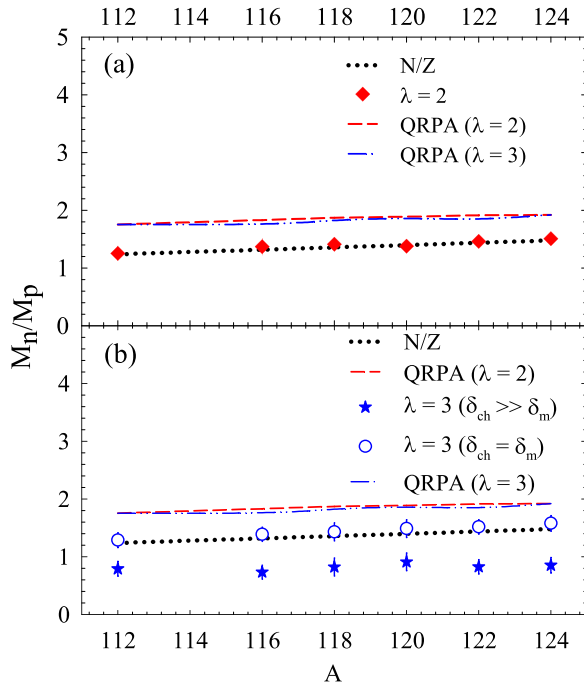[b]Present measurement.
[c]Modified.

FIG. 7. M_n/M_p ratios for low-lying excitations in Sn isotopes corresponding to (a) $\lambda = 2$ and (b) $\lambda = 3$. The dotted line shows the homogeneous isoscalar value of N/Z. The dashed and dash-dotted lines represent the results of QRPA calculations for 2^+ and 3^- transitions respectively.

and nuclear interactions, the large difference in M_n/M_p ratios compared to the measured values for both 2_1^+ as well as 3_1^- states may be a consequence of them.

For strongly absorbed probes, such as ^{7}Li, only the surface region of the Sn nuclei contributes to the direct reaction processes so that the scattering cross section in the regions of the Coulomb and nuclear fields is proportional to the respective matrix elements. The electromagnetic transition probability is directly related to the charge deformation, and in turn, the proton transition matrix element of a nucleus as $B(E\lambda) = |M_p|^2$. To decouple the presence of in-phase (homogeneous) and out-of-phase (inhomogeneous) vibrations of neutrons and protons in a transition, a similar quantity related to the mass deformation of the nucleus may be defined, in which neutrons and protons explicitly move in phase and retain the equilibrium density ratios, known as the isoscalar transition probability [4]

$$B(IS\lambda) = \left(\frac{Z}{A}\right)^2 |M_n + M_p|^2. \tag{4}$$

For $M_n/M_p = N/Z$, one obtains $B(IS\lambda) \equiv B(E\lambda)$. Using the results of M_n/M_p, the present $B(E\lambda)$ and $B(IS\lambda)$ values are shown in Tables IV and V. The errors on all the above quantities are assigned by propagating the errors on the corresponding δ_λ^{ch} and δ_λ^m values extracted from the model calculations. One observes that the $\lambda = 2$ vibration is a predominantly homogeneous mass vibration with similar $B(E2)$ and $B(IS2)$ values. A significant deviation is observed for

$\lambda = 3$ transition in Sn using δ_3^{ch} from pure electromagnetic measurement and δ_3^m from present study. This is reflected in the damped isoscalar transition probability, $B(IS3) \ll B(E3)$, owing to much lower collective M_n/M_p ratios. The mass deformation length across the chain of Sn isotopes is lower than existing estimates obtained from a variety of methods. Similar observations were made even for the low-lying excitations in ^{90}Zr [44], ^{94,98}Mo [45], and in neutron-excess oxygen [40] and sulfur isotopes [46]. The present results hint at a possible inhomogeneity for the octupole excitation in Sn when probed using ^{7}Li. The transition densities of neutrons and protons are not of the same radial shape when excitation to this state takes place, leading to damped isoscalar vibrations compared to previously observed parameters characterizing charge vibration. Considerable uncertainty in the result of Fig. 7(b) may arise due to lack of consistent electromagnetic data and ambiguity in the available choices for $B(E3)$ values. Each set predicts different M_n/M_p ratios. However, the net conclusion is found to remain unchanged.

V. SUMMARY

Differential cross sections for elastic scattering and first 2_1^+ and 3_1^- target excited states have been measured in the ^{7}Li + ^{112,116,118,120,122,124}Sn systems at 28 MeV beam energy and explained with CRC as well as CDCC-CRC calculations. The extracted $B(E2)$ values are consistent with existing measurements, with similar mass and charge deformation lengths. Reasonable agreement is seen between the proton and neutron deformation lengths for all isotopes leading to $M_n/M_p \sim N/Z$. As a result, the difference between proton and neutron transition densities is negligible. The cross section is entirely determined by the isoscalar form factor, identical to the Coulomb form factor. A simple collective model is usually adequate, normalized to give the observed $B(E2)$.

Unlike the 2_1^+ state, the mass (isoscalar) deformation length for the 3_1^- state in each Sn isotope is found to be much smaller than the values of deformation length obtained from existing measurements. This is also reflected in the much lower value of M_n/M_p ($\ll N/Z$) for this state, obtained by comparing the extracted mass deformation length with charge deformation length from pure electromagnetic measurements. The sensitivity of the differential cross section to δ_3^{ch} is found to be low. However, it greatly influences the ratio M_n/M_p. Moreover, δ_3^m was found to be nearly independent of δ_3^{ch}. The damped mass vibration could be a direct consequence of inhomogeneous oscillations of proton and neutron densities owing to the presence of neutron skin, which does not show up in the integrated $B(E3)$ values commonly obtained from homogeneous collective model calculations. Since the understanding of the pure electromagnetic excitation is well established, fresh measurements for a precise estimate of the octupole charge deformation lengths are highly crucial, to reduce such uncertainties in understanding the effects of nuclear skin, if any, on the mechanism of CNI in heavy ion scattering. The present considerations will be important when one discusses the deformation properties of the proton and neutron distributions in highly neutron-rich unstable nuclei, where the effect of the neutron skin is expected to be even larger.

[1] A. M. Bernstein, V. R. Brown, and V. A. Madsen, Phys. Lett. B **106**, 259 (1981).

[2] A. M. Bernstein, V. R. Brown, and V. A. Madsen, Comments Nucl. Part. Phys. **11**, 203 (1983).

[3] A. M. Bernstein, V. R. Brown, and V. A. Madsen, Phys. Lett. B **103**, 255 (1981).

[4] A. M. Bernstein, in *Advances in Nuclear Physics*, edited by M. Baranger and E. Vogt (Springer, Berlin, 1969), Vol. 3.

[5] B. Hrastnik, V. Knapp, and M. Vlatkovic, Nucl. Phys. **89**, 412 (1966).

[6] P. H. Stelson, F. K. McGowan, R. L. Robinson, and W. T. Milner, Phys. Rev. C **2**, 2015 (1970).

[7] R. Graetzer, S. M. Cohick, and J. X. Saladin, Phys. Rev. C **12**, 1462 (1975).

[8] J. Bryssinck, L. Govor, V. Y. Ponomarev, F. Bauwens, O. Beck, D. Belic, P. von Brentano, D. D. Frenne, T. Eckert, C. Fransen *et al.*, Phys. Rev. C **61**, 024309 (2000).

[9] J. M. Allmond, A. E. Stuchbery, A. Galindo-Uribarri, E. Padilla-Rodal, D. C. Radford, J. C. Batchelder, C. R. Bingham, M. E. Howard, J. F. Liang, B. Manning *et al.*, Phys. Rev. C **92**, 041303 (2015).

[10] R. Kumar, M. Saxena, P. Doornenbal, A. Jhingan, A. Banerjee, R. K. Bhowmik, S. Dutt, R. Garg, C. Joshi, V. Mishra *et al.*, Phys. Rev. C **96**, 054318 (2017).

[11] N. G. Jonsson, A. Backlin, J. Kantele, R. Julin, M. Luontarna, and A. Passoja, Nucl. Phys. A **371**, 333 (1981).

[12] R. H. Spear, A. M. Baxter, S. M. Burnett, and C. L. Miller, Aust. J. Phys. **42**, 41 (1989).

[13] T. H. Curtis, R. A. Eisenstein, D. W. Madsen, and C. K. Bockelman, Phys. Rev. **184**, 1162 (1969).

[14] P. Barreau and J. B. Bellicard, Phys. Rev. Lett. **19**, 1444 (1967).

[15] O. Beer, A. E. Behay, P. Lopato, Y. Terrien, G. Vallois, and K. K. Seth, Nucl. Phys. A **147**, 326 (1970).

[16] G. Bruge, J. C. Faivre, H. Faraggi, and A. Bussiere, Nucl. Phys. A **146**, 597 (1970).

[17] N. Baron, R. F. Leonard, J. L. Need, W. M. Stewart, and V. A. Madsen, Phys. Rev. **146**, 861 (1966).

[18] P. P. Singh, Q. Li, P. Schwandt, W. W. Jacobs, M. Saber, E. J. Stephenson, A. Saxena, and S. Kailas, Pramana - J. Phys. **27**, 747 (1986).

[19] A. Kundu, S. Santra, A. Pal, D. Chattopadhyay, R. Tripathi, B. J. Roy, T. N. Nag, B. K. Nayak, A. Saxena, and S. Kailas, Phys. Rev. C **95**, 034615 (2017).

[20] I. J. Thompson and F. M. Nunes, *Nuclear Reactions for Astrophysics* (Cambridge University Press, New York, 2009).

[21] J. Cook, A. K. Abdallah, M. N. Stephens, and K. W. Kemper, Phys. Rev. C **35**, 126 (1987).

[22] T. Davidson, V. Rapp, A. C. Shotter, D. Branford, M. A. Nagarajan, I. J. Thompson, and N. E. Sanderson, Phys. Lett. B **139**, 150 (1984).

[23] G. Tungate, D. Kramer, R. Butsch, O. Karban, K. H. Mobius, W. Ott, P. Paul, A. Weller, E. Steffens, and K. Becker, J. Phys. G: Nucl. Phys. **12**, 1001 (1986).

[24] M. Conjeaud, S. Harar, and Y. Cassagnou, Nucl. Phys. A **117**, 449 (1968).

[25] R. F. Casten, E. R. Flynn, O. Hansen, and T. J. Mulligan, Nucl. Phys. A **180**, 49 (1972).

[26] E. J. Schneid, A. Prakash, and B. L. Cohen, Phys. Rev. **156**, 1316 (1967).

[27] X. Chen, Y.-W. Lui, H. L. Clark, Y. Tokimoto, and D. H. Youngblood, Phys. Rev. C **76**, 054606 (2007).

[28] G. R. Satchler and W. G. Love, Phys. Rep. **55**, 183 (1979).

[29] D. T. Khoa, W. von Oertzen, and A. A. Ogloblin, Nucl. Phys. A **602**, 98 (1996).

[30] C. W. De Jager, H. De Vries, and C. De Vries, At. Data Nucl. Data Tables **14**, 479 (1974).

[31] I. Tanihata, T. Kobayashi, O. Yamakawa, S. Shimoura, K. Ekuni, K. Sugimoto, N. Takahashi, T. Shimoda, and H. Sato, Phys. Lett. B **206**, 592 (1988).

[32] S. Terashima, H. Sakaguchi, H. Takeda, T. Ishikawa, M. Itoh, T. Kawabata, T. Murakami, M. Uchida, Y. Yasuda, M. Yosoi *et al.*, Phys. Rev. C **77**, 024317 (2008).

[33] A. Krasznahorkay, A. Balanda, J. A. Bordewijk, S. Brandenburg, M. N. Harakeh, N. Kalantar-Nayestanaki, B. M. Nyako, J. Timar, and A. van der Woude, Nucl. Phys. A **567**, 521 (1994).

[34] F. G. Perey and G. R. Satchler, Nucl. Phys. A **97**, 515 (1967).

[35] N. Keeley (private communication).

[36] L. C. Chamon, B. V. Carlson, L. R. Gasques, D. Pereira, C. De Conti, M. A. G. Alvarez, M. S. Hussein, M. A. Cândido Ribeiro, E. S. Rossi, and C. P. Silva, Phys. Rev. C **66**, 014610 (2002).

[37] C. Beck, N. Keeley, and A. Diaz-Torres, Phys. Rev. C **75**, 054605 (2007).

[38] B. Buck and A. C. Merchant, J. Phys. G **14**, L211 (1988).

[39] D. T. Khoa and G. R. Satchler, Nucl. Phys. A **668**, 3 (2000).

[40] D. T. Khoa, Phys. Rev. C **68**, 011601 (2003).

[41] A. Bohr and B. R. Mottelson, *Nuclear Structure* (Benjamin, New York, 1975), Vol. 2.

[42] V. Yu. Ponomarev (private communication).

[43] V. G. Soloviev, *Theory of Atomic Nuclei: Quasiparticles and Phonons* (Institute of Physics Publishing, Bristol, 1992).

[44] Y. Wang and J. Rapaport, Nucl. Phys. A **517**, 301 (1990).

[45] G. M. Ukita, T. Borello-Lewin, L. B. Horodynski-Matsushigue, J. L. M. Duarte, and L. C. Gomes, Phys. Rev. C **64**, 014316 (2001).

[46] D. T. Khoa, E. Khan, G. Colo, and N. Van Giai, Nucl. Phys. A **706**, 61 (2002).